

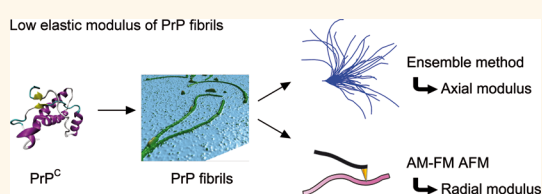
# High Intrinsic Mechanical Flexibility of Mouse Prion Nanofibrils Revealed by Measurements of Axial and Radial Young's Moduli

Guillaume Lamour,<sup>†,‡,§,\*</sup> Calvin K. Yip,<sup>§</sup> Hongbin Li,<sup>‡,\*</sup> and Jörg Gsponer<sup>†,§,\*</sup>

<sup>†</sup>Centre for High-Throughput Biology, University of British Columbia, Vancouver, BC, Canada V6T 1Z4, <sup>‡</sup>Department of Chemistry, University of British Columbia, Vancouver, BC, Canada V6T 1Z1, and <sup>§</sup>Department of Biochemistry & Molecular Biology, University of British Columbia, Vancouver, BC, Canada V6T 1Z3

**ABSTRACT** Self-templated protein aggregation and intracerebral deposition of aggregates, sometimes in the form of amyloid fibrils, is a hallmark of mammalian prion diseases. What distinguishes amyloid fibrils formed by prions from those formed by other proteins is not clear. On the basis of previous studies on yeast prions that correlated high intrinsic fragmentation rates of fibrils with prion propagation efficiency, it has been hypothesized that the nanomechanical

properties of prion amyloid such as strength and elastic modulus may be the distinguishing feature. Here, we reveal that fibrils formed by mammalian prions are relatively soft and clearly in a different class of rigidities when compared to nanofibrils formed by nonprions. We found that amyloid fibrils made of both wild-type and mutant mouse recombinant PrP(23-231) have remarkably low axial elastic moduli of 0.1–1.4 GPa. We demonstrate that even the proteinase K resistant core of these fibrils has similarly low intrinsic rigidities. Using a new mode of atomic force microscopy called AM-FM mode, we estimated the radial modulus of PrP fibrils at  $\sim 0.6$  GPa, consistent with the axial moduli derived by using an ensemble method. Our results have far-reaching implications for the understanding of protein-based infectivity and the design of amyloid biomaterials.



**KEYWORDS:** atomic force microscopy · prion · amyloid · Young's modulus · protein aggregation · AM-FM AFM · nanomechanics

Mammalian prions are infectious proteinaceous agents that can cause transmissible encephalopathies such as Creutzfeldt-Jacob disease in humans and mad cow disease in cattle.<sup>1</sup> Fundamental to these diseases is the conversion of an initially soluble, globular prion protein (PrP<sup>C</sup>) into a misfolded form (PrP<sup>Sc</sup>) that aggregates.<sup>2</sup> Prion-like replication of protein aggregates has also been found in yeast.<sup>3</sup> Like mammalian prions, yeast prions propagate in a polymerization process that is catalyzed by the aggregate state, *i.e.*, the misfolded and aggregated isoform of the prion catalyzes the conversion of the soluble isoform. Common to all forms of prions is the ability to form highly ordered protein aggregates, so-called amyloid fibrils. Several neurodegenerative diseases, including Alzheimer's, Parkinson's, or Huntington's disease, are also associated with the presence of amyloid fibrils in the brain of patients. However, whether these protein aggregates can also spread *via* a prion-like

mechanism is highly controversial.<sup>4–7</sup> Hence, what differentiates amyloids formed by *bona fide* prions from amyloids formed by other proteins is not well understood.

Recent studies indicate that nanomechanics may play an important role not only in the conversion process of soluble proteins into their fibrillar state, but especially in the key characteristics of prions: their transmissibility.<sup>8,9</sup> Amyloid fibrils are highly sensitive to local thermal fluctuations in liquid medium, which cause them to undergo bending along their longitudinal axis. When fibrils have low mechanical strength and grow very long, spontaneous fragmentation through these thermal fluctuations becomes more likely.<sup>10–12</sup> Most importantly, fragmentation creates free ends that have high seeding potential; *i.e.*, soluble monomers can add to the free fibril ends. This mechanism may be very important for prions, which normally have a very low rate of spontaneous *de novo* generation of fibrils, and therefore, fragmentation may

\* Address correspondence to lamour@chibi.ubc.ca, hongbin@chem.ubc.ca, gsponer@chibi.ubc.ca.

Received for review February 4, 2014 and accepted March 3, 2014.

Published online March 03, 2014  
10.1021/nn5007013

© 2014 American Chemical Society

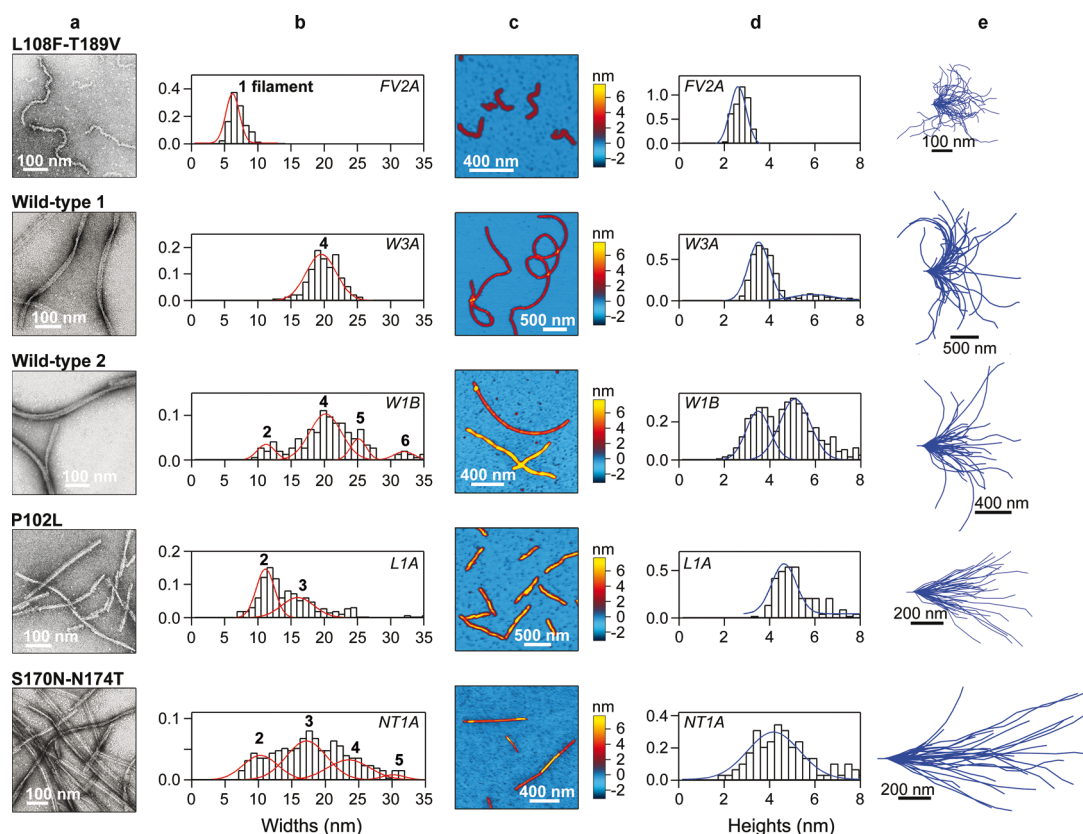


**Figure 1.** Morphological characteristics of prion nanofibrils. (a) Electron microscopy images of fibrils used to determine fibril widths. Nanofibrils exhibit ribbon morphology, including what appears to be single filaments (FV2A sample). In both wild-type samples, a fibril twist is apparent. (b) Normalized distribution of fibril widths. (c) Atomic force microscopy (AFM) images used to measure fibril heights. (d) Normalized distribution of fibril heights. Uncertainties related to heights and widths distributions can be found in the Supporting Information, Table S3. (e) Contours of fibrils imaged by AFM, where initial tangents were aligned to facilitate visualization.

provide enough new conversion and growth sites for prion propagation. Indeed, amyloid fibrils formed by the yeast prion Sup35 that have a low mechanical strength and a high intrinsic fragmentation rate have been shown to propagate most effectively as prions.<sup>8</sup> Interestingly, an inverse correlation has also been found between the thermodynamic stability of amyloid fibrils formed by recombinant PrP and the time before disease develops (incubation time).<sup>13</sup>

In this context, it appears mandatory to improve our understanding of the nanomechanics of amyloid fibrils, even more so as increasing efforts are made to use amyloids in designed biomaterials. Atomic force microscopy (AFM) is a tool that is particularly suited for this endeavor. Indeed, AFM has recently been used in a large number of studies that had as a focus the characterization of various aspects of amyloid properties, not only their nanomechanics. The nucleation process of amyloid formation,<sup>14,15</sup> filament and fibril assembly, and the topological characteristics and diversity of fibrils as a function of time and conditions<sup>16–19</sup> have successfully been investigated with the help of AFM. The nanomechanics have been investigated by different approaches, for instance by the AFM-based unzipping of functional amyloids<sup>20</sup> or the analysis of

AFM images of amyloid fibrils. The latter studies used statistical analysis of fibril bending to derive mechanical properties of fibrils formed by various proteins and peptides.<sup>21–23</sup> These studies demonstrated that mature nanofibrils have axial moduli between 2 and 14 GPa.

However, the nanomechanical properties of fibrils formed by PrP are not known. Here, we reveal that mature fibrillar cores formed by wild-type and mutant PrP are very distinct from amyloid fibrils formed by other nonprion proteins, as they have rather low intrinsic stiffness characterized by axial elastic moduli of 0.1–1.4 GPa. Our findings provide strong support for the hypothesis that high intrinsic flexibility is a key hallmark of nanofibrils formed by prions.

## RESULTS AND DISCUSSION

**Fibril Morphologies.** We generated and analyzed amyloid fibrils of wild-type (W) mouse prion protein PrP<sup>23–231</sup> as well as three mutants: P102L (L), S170N-N174T (NT), and L108F-T189V (FV). P102L is a mutation associated with the Gerstmann–Sträussler–Scheinker (GSS) phenotype, a familial form of Creutzfeldt–Jacob disease,<sup>24</sup> S170N and N174T were shown to cause transmissible *de novo* prion disease in transgenic mice,<sup>25</sup> and the L108F and T189V polymorphisms have

a strong impact on incubation time.<sup>26</sup> Moreover, these mutations are located within as well as outside the  $\beta$ -sheet-rich core (residues  $\sim$ 160–220) of fibrils formed by recombinant PrP (see Supporting Information Note S1).<sup>27,28</sup> Fibrils were grown in three different buffers,<sup>13,29</sup> as well as at different initial concentration, with or without seeds, and at different speeds and durations of shaking. Details of these experimental settings can be found in the Supporting Information, Table S1. The amyloid nature of the mature nanofibrils that we made was confirmed by FTIR spectroscopy (see Table S2, Figure S1, and Note S2 in the Supporting Information).

We analyzed morphological characteristics of the fibrils by electron microscopy (EM; Figure 1a) to measure widths (Figure 1b) and atomic force microscopy (AFM; Figure 1c) using AC mode in ambient air to measure heights (Figure 1d) and shapes (Figure 1e). The shape fluctuations of the fibrils were statistically analyzed using different equations derived from the worm-like chain model in order to determine the persistence length ( $P_L$ ). For instance,  $P_L$  was calculated by means of monitoring the mean square of the end-to-end distance  $R$ ,  $\langle R^2 \rangle = 4P_L / (1 - 2P_L / (1 - \exp(-L/2P_L)))$ , over distances  $L$  along the fibril contour (see Supplementary Methods in the Supporting Information for details). Measuring  $P_L$  is essential in order to characterize the elastic properties of the fibrils because  $P_L$  relates to the length above which the thermal energy can bend the fibril.

Figure 1 and Supporting Information Figures S2 and S3 show that a broad spectrum of fibril sizes and shapes can be observed for the different sequences of PrP as well as the varying fibrillation conditions; for instance, FV forms mainly fine filaments of heights between 2.5 and 3.5 nm, while NT forms mature fibrils of various heights, some of which have heights up to 10 nm. Fibrils with different cross sections have very different persistence lengths (Supporting Information, Tables S3 and S4). As PrP fibrils are known for their morphological heterogeneity,<sup>30,31</sup> it was important to make sure that the generated fibrils are homogeneous enough so that the persistence length varies as little as possible in a given sample. Most importantly, Figure 1 reveals that mutating PrP in only a few positions significantly altered the population of fibrils formed, which is reflected in varying cross-sectional dimensions and changes in persistence lengths of up to 175-fold (range of persistence lengths: 0.065–11.4  $\mu$ m).

**Axial Elastic Moduli Measurements.** Next, we determined the bending rigidity ( $B_R$ ) and cross-sectional second moment of area ( $I$ ) for the fibrils in each sample.  $B_R$  was calculated from the persistence length ( $B_R = P_L \times k_B T$ ) and  $I$  by using the measured heights and widths in a model that has ellipsoidal geometry of the cross-section, consistent with the morphologies of the vast majority of the fibrils, as displayed by EM images (see Supporting Information Note S3 for further details

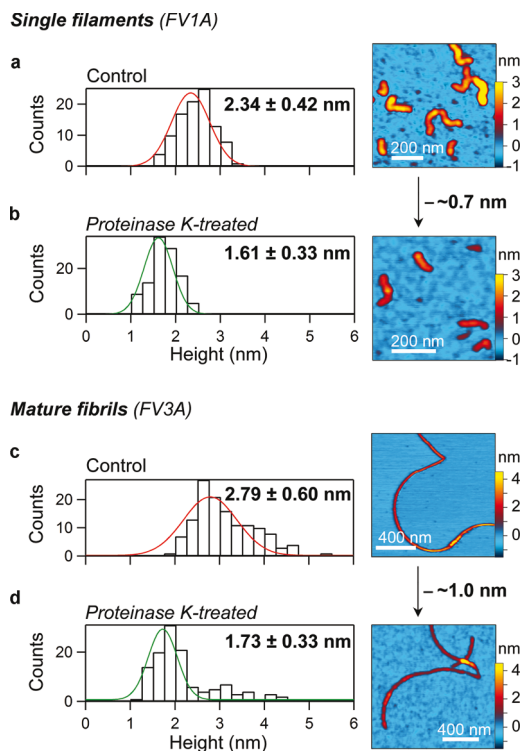


**Figure 2.** Effect of proteinase K (PK) treatment on prion nanofibril morphology: (a and b) single filament sample; (c and d) mature amyloid fibril sample; (a and c) heights distribution and AFM image in untreated fibrils; (b and d) heights distribution and AFM image in PK-treated fibrils. Experiments were performed *in situ*, that is, when fibrils were already adsorbed on mica (see Methods). Section analyzes were performed and counted peak heights reported in histograms in a and c.

on why the ellipsoidal model was selected). Using this model, we assessed the axial elastic modulus  $E = B_R / I$  of the fibrils. To consider in this calculation is that not all of PrP23–231 is part of the fibril core. Nonaggregated sequence parts, whether structured or unstructured, are likely to extend outward from the fibrillar core, forming the “hair” of the fibrils. Therefore, measured heights may be too large and derived cross-sectional second moments of area are likely overestimated. In other words, the entire cross section may not experience mechanical load.<sup>32</sup> To shed light on this, we treated four distinct fibril samples with proteinase K (PK), in order to have direct estimates of the contribution of the “hair” to the height of fibrils as measured by AFM. The height of the fibrils was reduced by 0.7–1.0 nm (Figure 2). Height reduction in single filaments was not significantly different from that in mature fibrils (Figure 2 and Supporting Information Figure S4), suggesting that at least some part of the “hair”, PK-inaccessible part, may be involved in holding filaments together in mature fibrils, and as such, contributing to the mechanical stability of the whole nanofibril.

The assessment of the effect of the “hair” allowed us to calculate the second moments of area using

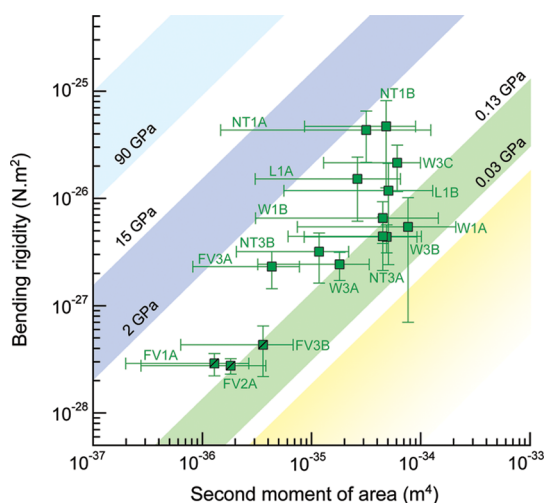


**Figure 3.** Axial elastic modulus of prion nanofibrils. Bending rigidity ( $B_R$ ) versus second moment of area  $I$  was plotted for various prion nanofibrils. An ellipsoidal model was used to calculate  $I$  for fibrils after PK treatment, *i.e.*, after correction of heights and widths for the “hair” effect (see Figures 2, and S4 and S5). Background coloring has been adapted from Knowles *et al.*<sup>21</sup> for comparison purposes. The light blue region is representative of materials held together by strong intermolecular forces such as covalent bonds in metals. The dark blue band represents a range of elastic moduli found for nonprion amyloid fibrils in previous studies.<sup>21,22</sup> The green band represents materials that are held together by amphiphilic interactions (see main text for definition) and the yellow band is the region corresponding to entropic elasticity. Data points crossed by diagonal bars represent filament samples, whereas the others are all mature amyloid fibrils.

corrected heights and widths (Figure 3 and Supporting Information Figure S5). Figure 3 shows  $B_R$  as a function of  $I$  for the ellipsoidal model and reveals that fibrils of all samples have moduli between 0.1 and 1.4 GPa, which is below the range previously determined for nonprion amyloid fibrils<sup>21,22</sup> (below the “blue” region, for which  $E = 2–14$  GPa). Indeed, many samples appear in the “green” region, representative of a range of intermolecular forces that correspond to amphiphilic interactions (defined as “intermolecular interactions that are mediated by the variable side chains in the absence of a rigid framework provided by intermolecular hydrogen bonding”<sup>21,32</sup>). This result is independent of the cross-sectional model used to calculate  $I$  (Supporting Information Figure S5). Although a relatively low Young's modulus may be expected for non-amyloid single filaments (marked by diagonal bars in the graph),<sup>21</sup> the fact that we obtained the same result for mature fibrils suggests that nanofibrils formed by PrP are intrinsically more flexible, *i.e.*, less resistant to bending, and clearly distinct from nanofibrils formed by other proteins and studied previously using the same method.<sup>21,22</sup>

**Robustness of the Approach.** Next, we sought to evaluate whether fibrils had time to equilibrate on the substrate (mica) or, conversely, were kinetically trapped in nonequilibrated conformations due to the high surface

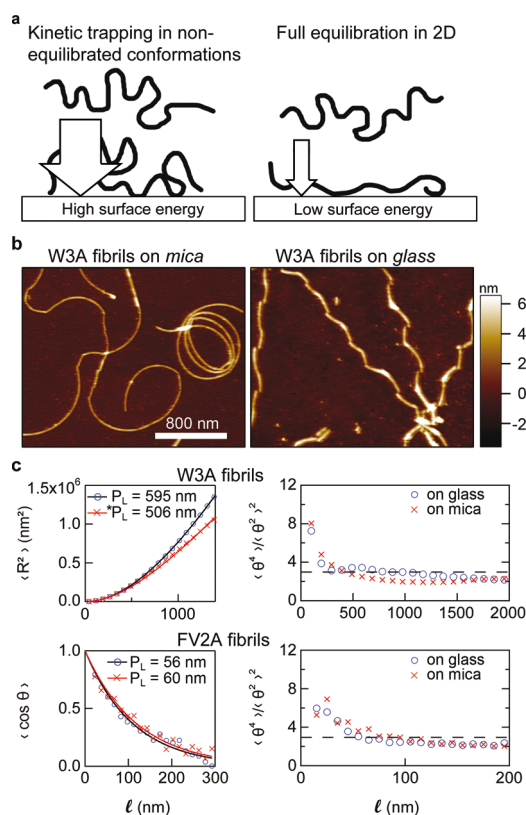


**Figure 4.** Influence of surface free-energy on fibril adsorption. (a) Schematics illustrating the differences in adsorption that occurs on a substrate with high surface energy (left panel) versus a substrate with low surface energy (right panel). The arrows exemplify the magnitude of long-range dispersion forces arising from the substrate, acting upon fibrils located in its vicinity. (b) AFM height images obtained in liquid tapping mode exemplifying the morphological differences between fibrils adsorbed on mica and on glass. (c) End-to-end distance ( $R$ ) and  $\cos \theta$  as a function of contour length for fibrils adsorbed on mica (red crosses) and glass (blue open circles) are shown on the left. Least-square fits to different forms of the worm-like chain model are shown as red and black lines, respectively. Persistence lengths ( $P_L$ ) derived from these fits are provided, with  $^*P_L$  indicating the value obtained from fitting the data using a model that takes into account the nonequilibrated state of fibril shape fluctuations (see Supporting Information, Supplementary Methods).  $\theta$  is the angle between two segments separated by a distance  $\ell$  along the fibril contour. The kurtosis of the  $\theta$  distribution as a function of  $\ell$  for fibrils adsorbed on mica (red crosses) and glass (blue open circles) is shown on the right. Only in the case of W3A fibrils adsorbed on mica, the kurtosis determined from experimental data (blue open circles and red crosses) is not very close to the theoretical value of 3 (broken line) and for  $\ell$  values in the range of  $P_L$ .

energy of the substrate, which will affect the derivation of persistence length. To do so, we first checked the adsorption of fibrils on glass and mica, which have surface free-energies of different magnitudes<sup>33–35</sup> (Figure 4a,b; see also Note S4 in the Supporting Information). If full equilibration in 2D occurs, derived persistence lengths  $P_L$  should be independent of the substrate used, while in the case of kinetic trapping, differences in  $P_L$  should be observed due to the higher surface free-energy of mica. Consistent with the latter,

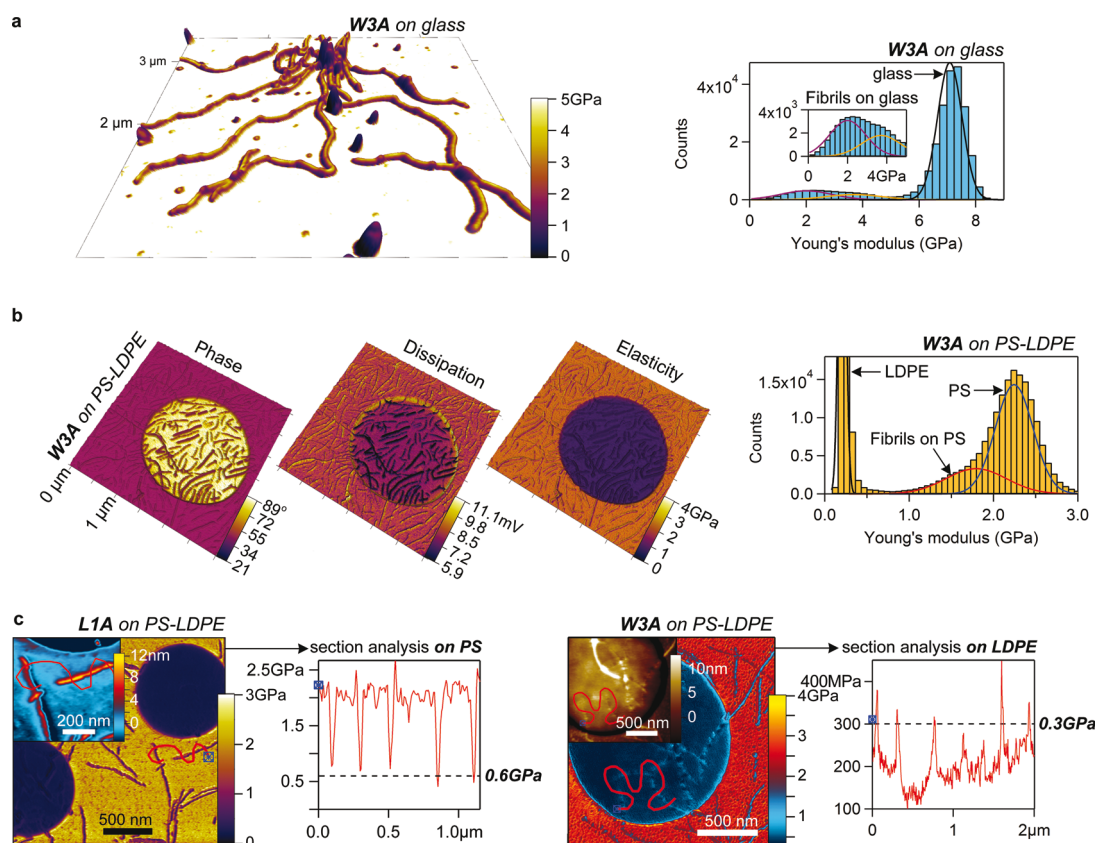


**Figure 5.** Radial elastic modulus of prion nanofibrils revealed by amplitude-modulation frequency-modulation (AM-FM) atomic force microscopy. (a) W3A fibrils on top of a glass surface. The elasticity map was overlaid on the 3D topographic representation. (Right graph) Histogram displaying moduli measured on the entire image. Heterogeneous fibril compliance is illustrated by the need of two combined Gaussians to fit the data in the inset of the graph. (b) W3A fibrils adsorbed on a calibration sample containing polystyrene and low-density polyethylene (PS-LDPE; LDPE is the circular area with lower E). Similar to (a), first resonance phase, second resonance (SR) amplitude, and SR frequency images were overlaid on top of the same 3D topographic representation of W3A fibrils. Whereas the phase signal of the first vibrational mode of the AFM cantilever results from a complex combination of adhesion forces, tip–sample contact stiffness, and energy dissipation, monitoring the resonant frequency and amplitude of the SR allows unambiguous decoupled imaging of sample elasticity and of tip–sample dissipation. (Right graph) Histogram displaying moduli distribution for all the pixels of the image. (c) Fibrils imaged on PS-LDPE and section analyzes on PS (left images) and on LDPE (right image), respectively.

persistence lengths derived from measurements on the two substrates are different for all samples (Figure 4c and Supporting Information, Figures S5 and S6) except the one with very flexible fibrils (FV2A sample:  $P_L \approx 65$  nm). We also checked whether the kurtosis, *i.e.*, the ratio of the even moments of the distribution of the angle  $\theta$ , resulted in  $\langle \theta^4(\angle) \rangle_{2D} / \langle \theta^2(\angle) \rangle_{2D}^2 = 3$ . For fibrils on glass, this ratio is very close to 3 (in the range of  $P_L$ ), which is consistent with a full equilibration of the fibrils in 2D.<sup>36</sup> In contrast, we concluded that the fibrils did not equilibrate in 2D on mica because the kurtosis never stayed close to 3. Therefore, the potential underestimation of persistence lengths that can occur when fibrils do not fully equilibrate on a 2D surface (see Supporting Information, Figure S6 and Note S4) was ruled out by considering a fractional dimension of  $2.5 \pm 0.5$  for all samples on mica, similar to the method used by Smith *et al.*<sup>22</sup>

We also determined that drying of the fibrils has no influence on the analysis (Supporting Information Figure S7). Parallel to this, it should be noted that W3A

fibrils on glass present noticeable undulations (Figure 4). However, these undulations do not jeopardize the analysis of bending rigidities because they occur at length scales smaller than the persistence length (see Supporting Information Figure S7d). Such undulations derive from the non-axisymmetric cross section of the fibrils combined with their twisting.<sup>37</sup> Finally, we confirmed the robustness of our approach (i) by measuring the persistence length and determining the Young's modulus of well-characterized insulin amyloid fibrils, for which we found an  $E \sim 3.2$  GPa (Supporting Information Figure S8a-c), consistent with previous reports<sup>21,22</sup> and (ii) by testing our code against synthetic polymers of known persistence lengths, generated by Monte Carlo simulations (see Methods). Overall, these controls confirm that amyloid fibrils formed by PrP have much lower rigidities than fibrils formed by non-prions that had been studied previously.<sup>21,22</sup>

**Radial Moduli Measurements.** To complete the description of the nanomechanical properties of PrP fibrils, we investigated their radial modulus, in addition to the

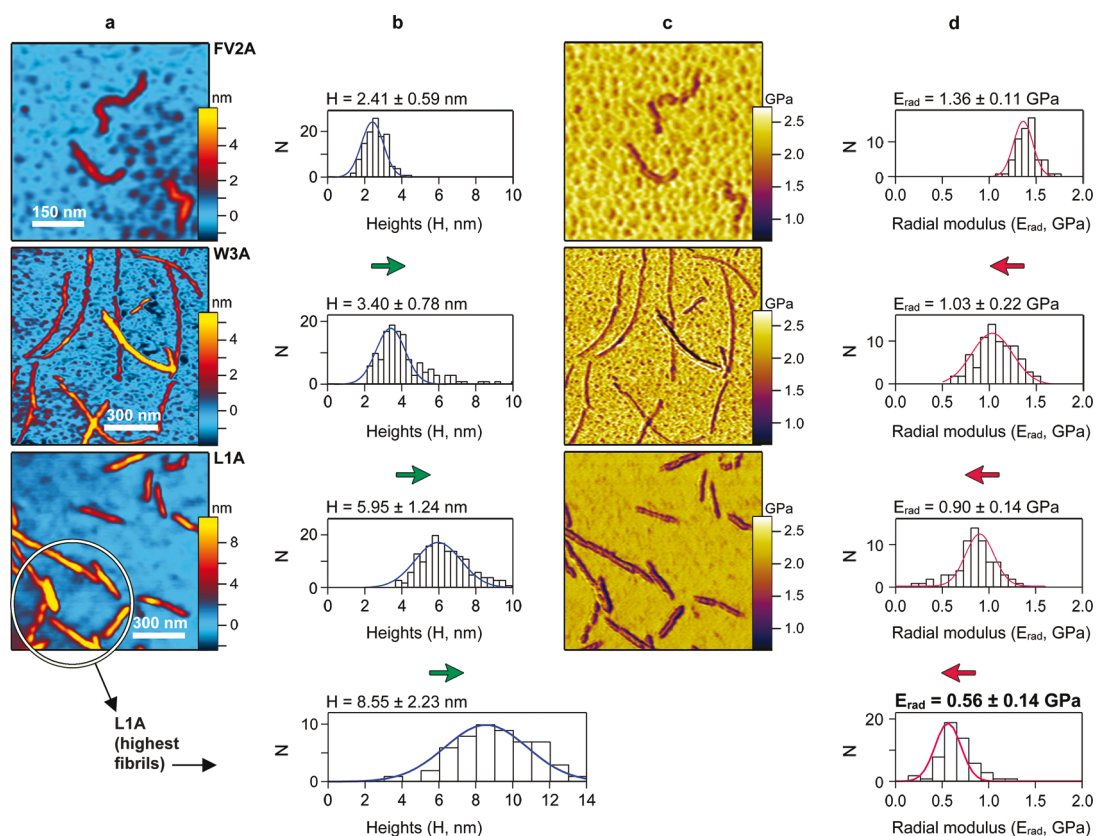


**Figure 6.** Inverse correlation between fibril height and fibril radial rigidity measured by AM-FM AFM. Prion nanofibril samples were imaged on a polystyrene-low density polyethylene (PS-LDPE) surface using a tip mounted on a cantilever with a spring constant of  $k \approx 2$  N/m. Elastic modulus ( $E$ ) maps were calibrated by setting  $E_{PS}$  at 2.2 GPa and  $E_{LDPE}$  at 0.2 GPa. (a) Topographical AFM images of fibrils on PS. (b) Histograms representing the distribution of heights in samples corresponding to AFM images in (a). For each fibril sample,  $N$  cross-sectional analyses of fibril diameters were performed on AFM images such as those displayed in (a) and counted. (c) Elastic modulus maps of the same fibrils imaged in (a) (both measurements were done simultaneously, see Methods). (d) Histograms of radial elastic moduli of fibrils measured  $N$  times in  $N$  cross-sectional analyzes using PS elastic modulus as background. Green and red arrows in (b) and (d) highlight the trend of lower radial moduli measured by AM-FM for fibrils with larger heights. (Bottom graphs) The highest L1A fibrils were selected and the height and the modulus of these fibrils measured simultaneously in cross-sectional analyzes.

axial modulus discussed above. The two moduli are expected to differ slightly because of the mechanical anisotropy of amyloid fibrils.<sup>38,39</sup> We used the new AFM technique called Amplitude-Modulation Frequency-Modulation (AM-FM) to determine the radial modulus. The basic principles of AM-FM AFM are illustrated in Supporting Information Figure S9 and explained in the Methods section. All prion fibril samples including single filaments displayed unexpectedly high radial moduli ( $E_{rad}$ ) of 2–4 GPa when imaged on mica or glass (Figure 5a, case of W3A fibrils). As fibrils are very thin (a few nanometers in diameter), it is probable that the high radial moduli recorded here is a consequence of the high moduli of the mica or glass surface ( $E > 60$  GPa). Due to relatively high amplitude of the first resonance oscillations, the tip indents and therefore “sees through” the fibril. For instance, this effect can be directly observed in Supporting Information Figure S9, where the fibril located at top-right corner of the image is displaying both lower height and higher radial modulus than the two other fibrils in the same image. Moreover, the radial modulus of glass is

estimated at  $\sim 7$  GPa in Figure 5a, which is a clear underestimation of its real value (see Methods).

To evaluate the dependence of the recorded moduli on the rigidity of the underlying surface, we analyzed fibrils directly adsorbed on the PS-LDPE calibration sample, which has well-defined moduli (Figure 5b, histogram). The  $E_{rad}$  is lower when fibrils are on PS compared to mica (Figure 5c: left image, and Figure 6. See also Figures S10, Notes S5 and S6 in the Supporting Information that further discuss AM-FM technical details). However, the dependence of  $E_{rad}$  on fibril height is still present on PS and highlighted in Figure 6. Therefore, we performed systematic cross-sectional analyzes of the highest fibrils available (subset of the L1A sample) and found a radial modulus of  $0.6 \pm 0.2$  GPa for fibrils with a height of  $8.6 \pm 2.2$  nm. This value is consistent with the axial modulus of the L1A sample (0.6 GPa) and the axial moduli of our fibrils (0.1–1.4 GPa). Comparisons with radial moduli that have been measured previously for nonprion amyloid fibrils are difficult because these measurements have been done mainly on mica and range from 5–50 MPa,<sup>40</sup>

to a few GPa.<sup>41,42</sup> Therefore, we measured the radial modulus of insulin amyloid fibrils on PS (Supporting Information Figure S8e). We found that their radial modulus is comparable to that of prion fibrils, with a radial modulus of  $E_{\text{rad}} \sim 1.3$  GPa on PS for fibrils with a height of  $2.1 \pm 0.8$  nm. Overall, our measurements of the radial modulus of mammalian prion fibrils indicate that it does not differ significantly from the radial modulus of other nonprion amyloid such as insulin fibrils. This finding contrasts the difference observed for the axial modulus (determined using an ensemble method that is not affected by tip indentation through the sample). It suggests that the mechanical anisotropy is higher in insulin fibrils than in prion fibrils.

## CONCLUSIONS

We generated prion nanofibrils displaying a broad range of bending rigidities and demonstrated that amyloid fibrils made from mammalian prion protein form very soft materials, especially in terms of monomers packing along the longitudinal axis of the fibrils. Their Young's modulus was found to be within 0.07–1.37 GPa. Consistent with these results, the axial elastic modulus of amyloids formed by the yeast prion protein Sup35 was recently found to be between 0.35–0.8 GPa.<sup>43</sup> These moduli are lower than the 2–14 GPa that were determined for amyloids formed by many other proteins that are not prions.<sup>21,22</sup> The highest moduli have been found for amyloid fibrils formed by short peptides.<sup>21,44</sup> *In silico* studies of the nanomechanics of fibril models formed by these peptides indicate that their high moduli arise from dense networks of backbone hydrogen bonds and “zipper-like” interactions of side chains in the core of the fibril structure.<sup>21,45,46</sup> It is believed that for longer polypeptide chains, which form fibrils with lower moduli,<sup>21</sup> it is

more difficult to find amyloid structures that accommodate all residues in strong intermolecular interactions. Polypeptides are known to be able to adopt different  $\beta$ -strand and  $\beta$ -sheet arrangements in amyloid fibrils<sup>47–49</sup> which in turn affect their nanomechanical properties<sup>50–52</sup> and biological effects.<sup>8,53</sup> In this context, one may speculate that the low elastic moduli of fibrils formed by mammalian prions indicate increased structural disorder and fewer strong intermolecular interactions when compared to other fibrils. More structural studies on PrP fibrils<sup>29,31,54–56</sup> are necessary to validate this hypothesis and correlate the different elastic moduli of mutants with structural differences.

In any case, our findings demonstrate that prion nanofibrils are exceptional amyloids with nanomechanical properties that are unique. Indeed, prion fibril cores are not only resistant to proteases such as PK but also less stiff than other non-amyloid filaments deprived of cross- $\beta$  sheets, such as actin filaments (Young's modulus  $E \sim 1.8$ – $2.6$  GPa),<sup>57,58</sup> microtubules ( $E \sim 1.2$  GPa),<sup>58</sup> or collagen fibers ( $E \sim 0.9$  GPa).<sup>59</sup> It remains to be determined how the compliance of prion fibrils influences the susceptibility to fragmentation compared to other amyloids formed by non-prions. As differences in fibril brittleness have been shown to affect prion propagation efficiency,<sup>8</sup> one may speculate that a low axial elastic modulus is another defining feature of efficiently propagating amyloids.<sup>60,61</sup> However, more studies are required to consolidate the link between fibril nanomechanics and propagation efficiency, and establish whether there exists a threshold value for the elastic modulus below which the propagation of amyloids made of recombinant proteins becomes as efficient as that of prions derived from infectious *in vivo* material.

## METHODS

**Preparation of Amyloid Fibrils.** Mouse PrP<sup>C</sup> (both wild-type and mutant) was expressed and purified by the PrionNet Prion Protein & Plasmid Production Platform Facility and amyloid fibrils prepared from PrP<sup>C</sup> (refer to Supporting Information for details on expression and purification protocols). Lyophilized prion protein was resuspended in 5 M GdnHCl at 5  $\mu\text{g}/\text{mL}$  and left to equilibrate at room temperature for 1 h. Meanwhile fresh buffer solutions were prepared, pH-adjusted, and sterile filtered using membranes with 0.22  $\mu\text{m}$ -diameter pores. Details on buffer compositions can be found in legend of Supporting Information Table S1 that recapitulates all experimental conditions used to manufacture all the prion nanofibril samples used in this study. Mixtures of buffer and protein stock solutions were adjusted to make a total volume of 400  $\mu\text{L}$  in each Eppendorf tube. These tubes were then placed horizontally and fixed by tape on top of a shaker plate at 37  $^{\circ}\text{C}$ . To promote fibril formation, tubes were shaken at rotation speeds and durations as indicated in Supporting Information Table S1. After fibril formation, a few microliters of fibril solution were diluted and the presence of fibrils was tested by atomic force microscopy (see below). Once checked for fibril presence, solutions were dialyzed in 25 mM sodium acetate buffer (pH 5.2) and 0.01%

$\text{NaN}_3$  (m/v) and stored at 4  $^{\circ}\text{C}$ . For control experiments, “standard” amyloid fibrils were prepared from 51-residue insulin as described previously.<sup>21</sup> Bovine insulin (Sigma) was dissolved in  $\text{H}_2\text{O}/\text{HCl}$  solution (pH = 2.0) at a concentration of 10 mg/mL. The tube was heated at 70  $^{\circ}\text{C}$  for 24 h, left at room temperature for 7 days, and then stored at 4  $^{\circ}\text{C}$ . In control experiments, FTIR spectra of several fibrils samples were recorded (experimental details on FTIR spectroscopy can be found in the Supporting Information, Supplementary Methods).

**AC Mode Atomic Force Microscopy (AFM).** Unless otherwise specified in the text, all fibril samples were analyzed on mica using an Asylum Research (Santa Barbara, CA) Cypher AFM in tapping (AC) mode in ambient air and AC160TS tip cantilevers from Olympus (nominal spring constant:  $k = 42$  N/m). For AC mode in liquid, we used TR400PB tip cantilevers (also from Olympus;  $k = 0.09$  N/m). Fibril solutions were diluted in 25 mM sodium acetate (pH 5.2) down to a concentration of  $\sim 5$ – $15$   $\mu\text{g}/\text{mL}$  (in monomer-equivalent molarity, it corresponds to  $\sim 0.2$ – $0.6$   $\mu\text{M}$ ). Twenty microliters of this diluted solution was spotted on freshly cleaved mica surface and left for fibrils to adsorb. After 5–15 min, substrates were gently rinsed at least 3 times with ultrapure water and then left to dry under a laminar flow hood or under moderate nitrogen stream. When glass was used as a

substrate, it was cleaned with piranha solution prior to fibril seeding [piranha solution is 3:1 (v/v) concentrated sulphuric acid/30% hydrogen peroxide (*Caution! Piranha solution is extremely explosive in presence of organic compounds; gloves, goggles, and a face shield should be worn*)], then thoroughly rinsed with ultrapure water and dried under a nitrogen stream. Glass coverslips were purchased from Ted Pella, Inc. In AFM experiments performed in liquid, the same seeding protocol as above was used, except that the substrates were not allowed to dry after water rinsing but instead covered by 100–150  $\mu\text{L}$  solution of 25 mM sodium acetate (pH 5.2).

For each sample, 43–253 fibrils were imaged (see Supporting Information Table S3). Scanning speeds of 3–6 Hz were used to collect images of 256–1024  $\times$  256–1024 pixels in standard AC mode with a scanning area of 0.5–5.0  $\mu\text{m}$   $\times$  0.5–5.0  $\mu\text{m}$ . As the AFM tip convolution effect (that decreases lateral resolution but does not affect measured heights) is not critical in our experiments, we used the same tip to collect a large number of images ( $N = 20$ –80). Piezoelectric Z-tube was driven to shake at a frequency slightly below the resonant frequency of the cantilever to favor imaging in repulsive mode, characterized by a phase lower than 90° (see Supporting Information Figure S7). The free air oscillation amplitude ( $A_0$ ) was set at 1–1.2 V and the drive set point ( $A_1$ ) at 700–800 mV. In liquid,  $A_0$  was often increased up to 4–5 V and the drive set point was decreased down to 300–400 mV to ensure imaging in repulsive mode. Keeping repulsive tip–sample interactions insures good surface tracking, stabilizing feedback operation by the AFM controller. Furthermore, it guarantees that height measurements are not overestimated, which is particularly important in our experiments. We checked that Z measurements were correctly calibrated using calibration grade (from Asylum Research) displaying steps of 200 nm. All fibril samples displayed in Figure 1 and Supporting Information Figures S2 and S3 were imaged within a few weeks after being prepared. In all images, the background topographical data corresponding to mica surface was flattened using the AFM software.

**AM-FM AFM.** Amplitude Modulation-Frequency Modulation (AM-FM) AFM is a recent technology developed at Asylum Research. Although different in essence than techniques such as pulsed force microscopy (PFM)<sup>62</sup> or peak force quantitative nanomechanical (QNM) AFM,<sup>41,42</sup> where the feedback is based on maximum force load, it also allows quantitative mapping of sample elasticity, at the relatively high scanning speed of conventional AC mode. AM-FM AFM is based on simultaneous monitoring of two distinct normal modes of vibration of the cantilever. Briefly, the first resonance is monitored as in standard tapping mode (also called AM or AC), returning sample topography through feedback on the first-resonance amplitude. Meanwhile the cantilever is driven to oscillate at a second resonance (SR), the frequency of which will be tracked by the controller. Simply put, a stiffer sample will shift the oscillation of that higher normal mode to a higher resonant frequency.<sup>63–65</sup> Hence, a quantitative elasticity map can be obtained together with dissipation map (acquired by monitoring the SR amplitude) that is related to the loss modulus of the sample (see Figure 5b). A great advantage of the technique is that no complex model of tip–sample contact mechanics, which would normally require assumptions on tip shape and size, is required. In fact, tip shape and size can be derived out of the equations, provided the experimentalist calibrates tip–sample interactions appropriately using samples with known elastic moduli (see Supplementary Methods for details).

In this study, AM-FM AFM was used to estimate the radial elastic modulus of prion nanofibrils. In experiments, we used AC160TS ( $k = 40$  N/m) and AC240TS ( $k = 2$  N/m) tip cantilevers (Olympus). The tip was brought in contact with the sample, and the drive frequency was carefully adjusted to the resonant frequency ( $f$ ) of the first normal mode of vibration of the cantilever, with the free air amplitude  $A_0 = 2$  V when using AC160TS ( $f_1 \approx 300$  kHz), and  $A_0 = 4$ –5 V using AC240TS ( $f_1 \approx 70$  kHz). Meanwhile, the cantilever was driven at a second resonance, characterized by higher frequency, corresponding to the second normal mode for AC160TS ( $f_2 \approx 1.8$  MHz) or to the third normal mode for AC240TS ( $f_2 \approx 1.2$  MHz). The second

mode was adjusted to keep the phase at 90°, on resonance. After the cantilever was calibrated using samples of known modulus, the tip was retracted and the calibration sample was removed, to be replaced by the sample of interest. When the tip-to-surface approach was completed, both resonances were tuned again and no other parameters (such as scanning speed or drive amplitude) changed until the sample was imaged. The drive set point of first normal mode was 700–800 mV, and that of the higher mode was 20–50 mV. A low ratio  $A_1/A_0$  ensured optimal tracking of the surface topography, which is critical to obtain proper results in AM-FM AFM. We note that the measurable positive shift in frequency in an AM-FM AFM experiment is limited. Therefore, experimental samples that are much stiffer than the calibration sample will look softer than they really are. Indeed, mica as well as glass ( $E > 60$  GPa) typically appear to have elastic moduli of  $\sim 4$ –7 GPa in such an AM-FM AFM experiment. We obtained the same values ( $\sim 4$ –7 GPa) for another sample made of Highly-Ordered Pyrolytic Graphite (HOPG, Bruker,  $E \approx 18$  GPa). Therefore, we hypothesize that any sample that has an elastic modulus over 7 GPa will appear to have a modulus of 4–7 GPa under the same calibration conditions that we used here.

For the determination of the elastic modulus of a sample, the user can choose between: (i) plotting the histogram of the distribution of the moduli recorded for all pixels of the image (see Figure 5a,b), or (ii) performing section analyzes that focus on precise locations in the image (see Figure 5c). When the distributions of the moduli measured for the substrate and fibril peak at clearly distinct values (see Figure 5a), the first method can be used although for small objects, like fibrils, very precise measurement can hardly be obtained. Indeed, it is more appropriate to use the second method, because the fibril's modulus is measured best at the highest point of the fibril, where substrate influence is minimized. Therefore, all radial moduli measurements in this study (excepting those on glass or mica) were obtained by measuring the moduli from cross sections performed at different points of several fibrils in several images. The values collected were then plotted as distributions of moduli in histograms (as in Figure 6).

**Transmission Electron Microscopy.** Fibril samples were adsorbed to glow discharged carbon-coated copper grids and stained with uranyl formate as previously described.<sup>66</sup> Specimens were examined using a Tecnai Spirit transmission electron microscope (FEI) equipped with a LaB6 filament and operated at an accelerating voltage of 120 kV. Images used for analysis were acquired at a nominal magnification of 49 000 $\times$  on a 4K  $\times$  4K Eagle charge-coupled device (CCD) camera (FEI). Fibril samples FV1A, FV2A, FV3A, FV3B, W1B, W3A, and W3B were imaged within 5 weeks after they were prepared. NT1B, NT3B, and L1B were imaged about 6 months after. NT1A, NT3A, L1A, and W1A were imaged about 9 months after. W1B and W3C were imaged about 12 months after. FV3B was imaged 18 months after. In the latter case, it is very interesting to note that, after such prolonged period of storage, single filaments that constitute the bulk of this particular sample were stable enough not to undergo spontaneous aggregation in more mature forms of fibrils.

**Statistical Analysis of Fibril Shape Fluctuations.** Persistence lengths ( $P_L$ ) of the fibrils were determined using different expressions derived from the worm-like chain (WLC) model for semiflexible polymers that undergo thermal bending. In short, using AFM heightmaps we fitted the contour of fibrils to parametric splines. These were then used to calculate, over distances  $l$  along the fibril contour and as a function of  $l$ , the mean-square end-to-end-distance ( $\langle R^2 \rangle$ ), the decay of tangent–tangent correlations ( $\langle \cos \theta \rangle$ ), where  $\theta$  is the angle between two segments of the fibril spline separated by  $l$ , and the mean square deviations ( $\langle \delta^2 \rangle$ ) from the midpoint of a secant joining two knots of the fibril spline. Importantly, we used measures describing polymer shape fluctuations in 2 dimensions for samples on glass only, and the midpoint between 2D and 3D fluctuations for samples on mica (as in Smith *et al.*<sup>22</sup>), in order not to underestimate  $P_L$ . Axial elastic moduli  $E$  were obtained by using  $E = P_L k_B T / I$ , where  $T$  is the room temperature,  $k_B$  is the Boltzmann constant, and  $I$  is the cross-sectional second moment of area of the fibrils.  $I$  was calculated from fibril height and width, respectively, obtained

by AFM and EM imaging. A complete description of various models used to determine  $P_L$  and  $l$  can be found in the Supporting Information.

**Treatment of Fibrils with Proteinase K.** Four fibril samples were treated with proteinase K (PK, from Sigma-Aldrich): FV1A, FV3A, W3A, and L1A. PK stock solution of 1 mg/mL in water was prepared. Fibril samples were adsorbed on mica surfaces as described above. After rinsing with ultrapure water, 60  $\mu$ L of a solution of 16  $\mu$ g/mL PK in 25 mM sodium acetate (pH 5.2) was dropped on the sample surfaces before they had started to dry. Control samples were immersed in 60  $\mu$ L of PK-free buffer. All samples were left in an incubator at 37 °C for 2.5 h. Then, samples were rinsed with water and gently dried under  $N_2$  flux prior to AFM imaging. In control experiments, fibrils were treated in solution prior to adsorption on mica, but in this case, PK concentration had to be dramatically reduced (down to 0.4  $\mu$ g/mL, corresponding to a mass ratio of approximately 1:50, as in Lee *et al.*<sup>31</sup>) to be able to image some of the nanofibrils (FV1A, FV3A, and L1A, but not W3A), that is, when they displayed a relatively even surface distribution. No fibrils could be suitably adsorbed and, thence, observed by AFM after immersion of samples in the same solution was prolonged overnight, suggesting that PK activity triggered fibril aggregation, even at such low concentration.

**Conflict of Interest:** The authors declare no competing financial interest.

**Acknowledgment.** Special thanks are due to Dr. David Wishart, head of PrP5 (PrionNet Prion Protein & Plasmid Production Platform Facility) as well as to Dr. Carol Ladner, Bow Suriyamongkol, and Ashenafi Abera, also at PrP5, for providing great assistance in producing prion protein. We thank Dheva Setiaputra for assistance in TEM imaging. Present study was funded by PrionNet Canada, the Canadian Institutes of Health Research, and the Natural Sciences and Engineering Research Council of Canada.

**Supporting Information Available:** Supplementary methods, Figures S1–S10, Tables S1–S4, and Notes S1–S6. Figure S1, the amyloid nature of mouse prion nanofibrils confirmed by FTIR spectroscopy. Figure S2, morphological characteristics of all nanofibrils made from MoPrP(23-231)-wild-type (W) and MoPrP(23-231)-P102L (L); Figure S3, morphological characteristics of all nanofibrils made from MoPrP(23-231)-L108F-T189V (FV) and MoPrP(23-231)-S170N-N174T (NT); Figure S4, influence of proteinase K (PK) treatment on fibril heights measured by atomic force microscopy; Figure S5, axial Young's modulus of prion nanofibrils calculated for 3 models of the fibril cross section; Figure S6, evidence for equilibrated and nonequilibrated conformations of different fibrils on the 2D surface; Figure S7, comparison of AC mode AFM performed in ambient air and in liquid medium; Figure S8, control measurements of Young's modulus of elasticity of "standard" amyloid fibrils made of insulin. Figure S9, schematics illustrating the physical basis of the AM-FM AFM technology; Figure S10, influence of the spring constant of the AFM cantilever on AM-FM AFM imaging of prion nanofibrils on a PS-LDPE surface. Table S1, summary of fibril samples; Table S2, peak attribution and distribution of secondary structure content determined from fitting and deconvoluting the FTIR amide I' band; Table S3, morphological and mechanical parameters used in the determination of the axial elastic modulus for each sample; Table S4, details of the thermal fluctuations analysis. Note S1, selection of mutants; Note S2, interpretation of FTIR spectra in Figure S1; Note S3, selection of the cross-sectional geometry of the fibrils; Note S4, comment on the trapping of fibrils in nonequilibrated conformations; Note S5, AM-FM AFM "see through" effect; Note S6, comment on the AM-FM AFM imaging of fibrils on LDPE islands. This material is available free of charge via the Internet at <http://pubs.acs.org>.

## REFERENCES AND NOTES

- Aguzzi, A.; Heikenwalder, M.; Polymenidou, M. Mechanisms of Disease—Insights into Prion Strains and Neurotoxicity. *Nat. Rev. Mol. Cell Biol.* **2007**, *8*, 552–561.

- Prusiner, S. B. Prions. *Proc. Natl. Acad. Sci. U. S. A.* **1998**, *95*, 13363–13383.
- Tessier, P. M.; Lindquist, S. Unraveling Infectious Structures, Strain Variants and Species Barriers for the Yeast Prion PSI<sup>+</sup>. *Nat. Struct. Mol. Biol.* **2009**, *16*, 598–605.
- Aguzzi, A. Cell Biology: Beyond the Prion Principle. *Nature* **2009**, *459*, 924–925.
- Brundin, P.; Melki, R.; Kopito, R. Prion-like Transmission of Protein Aggregates in Neurodegenerative Diseases. *Nat. Rev. Mol. Cell Biol.* **2010**, *11*, 301–307.
- Soto, C.; Estrada, L. D. Protein Misfolding and Neurodegeneration. *Arch. Neurol. (Chicago)* **2008**, *65*, 184–189.
- Westermarck, G. T.; Westermarck, P. Prion-like Aggregates: Infectious Agents in Human Disease. *Trends Mol. Med.* **2010**, *16*, 501–507.
- Tanaka, M.; Collins, S. R.; Toyama, B. H.; Weissman, J. S. The Physical Basis of How Prion Conformations Determine Strain Phenotypes. *Nature* **2006**, *442*, 585–589.
- Knowles, T. P. J.; Buehler, M. J. Nanomechanics of Functional and Pathological Amyloid Materials. *Nat. Nanotechnol.* **2011**, *6*, 469–479.
- Keten, S.; Xu, Z. P.; Ihle, B.; Buehler, M. J. Nanoconfinement Controls Stiffness, Strength and Mechanical Toughness of Beta-Sheet Crystals in Silk. *Nat. Mater.* **2010**, *9*, 359–367.
- Paparcone, R.; Buehler, M. J. Failure of A $\beta$ (1–40) Amyloid Fibrils under Tensile Loading. *Biomaterials* **2011**, *32*, 3367–3374.
- Xu, Z. P.; Paparcone, R.; Buehler, M. J. Alzheimer's A $\beta$ (1–40) Amyloid Fibrils Feature Size-Dependent Mechanical Properties. *Biophys. J.* **2010**, *98*, 2053–2062.
- Colby, D. W.; Giles, K.; Legname, G.; Wille, H.; Baskakov, I. V.; DeArmond, S. J.; Prusiner, S. B. Design and Construction of Diverse Mammalian Prion Strains. *Proc. Natl. Acad. Sci. U. S. A.* **2009**, *106*, 20417–20422.
- Varongchayakul, N.; Johnson, S.; Quabili, T.; Cappello, J.; Ghandehari, H.; Solares, S. D.; Hwang, W.; Seog, J. Direct Observation of Amyloid Nucleation under Nanomechanical Stretching. *ACS Nano* **2013**, *7*, 7734–7743.
- Cho, K. R.; Huang, Y.; Yu, S.; Yin, S.; Plomp, M.; Qiu, S. R.; Lakshminarayanan, R.; Moradian-Oldak, J.; Sy, M.S.; De Yoreo, J. J. A Multistage Pathway for Human Prion Protein Aggregation *In Vitro*: From Multimeric Seeds to Beta-Oligomers and Nonfibrillar Structures. *J. Am. Chem. Soc.* **2011**, *133*, 8586–8593.
- Sweers, K. K. M.; van der Werf, K. O.; Bennink, M. L.; Subramaniam, V. Atomic Force Microscopy under Controlled Conditions Reveals Structure of C-Terminal Region of Alpha-Synuclein in Amyloid Fibrils. *ACS Nano* **2012**, *6*, 5952–5960.
- Volpatti, L. R.; Vendruscolo, M.; Dobson, C. M.; Knowles, T. P. J. A Clear View of Polymorphism, Twist, and Chirality in Amyloid Fibril Formation. *ACS Nano* **2013**, *7*, 10443–10448.
- Ridgley, D. M.; Barone, J. R. Evolution of the Amyloid Fiber over Multiple Length Scales. *ACS Nano* **2013**, *7*, 1006–1015.
- Usov, I.; Adamcik, J.; Mezzenga, R. Polymorphism Complexity and Handedness Inversion in Serum Albumin Amyloid Fibrils. *ACS Nano* **2013**, *7*, 10465–10474.
- Alsteens, D.; Ramsook, C. B.; Lipke, P. N.; Duffrene, Y. F. Unzipping a Functional Microbial Amyloid. *ACS Nano* **2012**, *6*, 7703–7711.
- Knowles, T. P. J.; Fitzpatrick, A. W.; Meehan, S.; Mott, H. R.; Vendruscolo, M.; Dobson, C. M.; Welland, M. E. Role of Intermolecular Forces in Defining Material Properties of Protein Nanofibrils. *Science* **2007**, *318*, 1900–1903.
- Smith, J. F.; Knowles, T. P. J.; Dobson, C. M.; MacPhee, C. E.; Welland, M. E. Characterization of the Nanoscale Properties of Individual Amyloid Fibrils. *Proc. Natl. Acad. Sci. U. S. A.* **2006**, *103*, 15806–15811.
- Adamcik, J.; Jung, J. M.; Flakowski, J.; De Los Rios, P.; Dietler, G.; Mezzenga, R. Understanding Amyloid Aggregation by Statistical Analysis of Atomic Force Microscopy Images. *Nat. Nanotechnol.* **2010**, *5*, 423–428.
- Webb, T. E. F.; Poulter, M.; Beck, J.; Uphill, J.; Adamson, G.; Campbell, T.; Linehan, J.; Powell, C.; Brandner, S.; Pal, S.; *et al.*

- Phenotypic Heterogeneity and Genetic Modification of P102L Inherited Prion Disease in an International Series. *Brain* **2008**, *131*, 2632–2646.
25. Sigurdson, C. J.; Joshi-Barr, S.; Bett, C.; Winson, O.; Manco, G.; Schwarz, P.; Rulicke, T.; Nilsson, K. P. R.; Margalith, I.; Raeber, A.; *et al.* Spongiform Encephalopathy in Transgenic Mice Expressing a Point Mutation in the Beta 2-Alpha 2 Loop of the Prion Protein. *J. Neurosci.* **2011**, *31*, 13840–13847.
  26. Barron, R. M.; Baybutt, H.; Tuzi, N. L.; McCormack, J.; King, D.; Moore, R. C.; Melton, D. W.; Manson, J. C. Polymorphisms at Codons 108 and 189 in Murine PrP Play Distinct Roles in the Control of Scrapie Incubation Time. *J. Gen. Virol.* **2005**, *86*, 859–868.
  27. Lu, X. J.; Wintrode, P. L.; Surewicz, W. K. Beta-Sheet Core of Human Prion Protein Amyloid Fibrils as Determined by Hydrogen/Deuterium Exchange. *Proc. Natl. Acad. Sci. U. S. A.* **2007**, *104*, 1510–1515.
  28. Ganchev, D. N.; Cobb, N. J.; Surewicz, K.; Surewicz, W. K. Nanomechanical Properties of Human Prion Protein Amyloid as Probed by Force Spectroscopy. *Biophys. J.* **2008**, *95*, 2909–2915.
  29. Lee, Y. J.; Savtchenko, R.; Ostapchenko, V. G.; Makarava, N.; Baskakov, I. V. Molecular Structure of Amyloid Fibrils Controls the Relationship between Fibrillar Size and Toxicity. *PLoS One* **2011**, *6*, e20244.
  30. Jones, E. M.; Surewicz, W. K. Fibril Conformation as the Basis of Species- and Strain-Dependent Seeding Specificity of Mammalian Prion Amyloids. *Cell* **2005**, *121*, 63–72.
  31. Anderson, M.; Bocharova, O. V.; Makarava, N.; Breydo, L.; Salnikov, V. V.; Baskakov, I. V. Polymorphism and Ultrastructural Organization of Prion Protein Amyloid Fibrils: An Insight from High Resolution Atomic Force Microscopy. *J. Mol. Biol.* **2006**, *358*, 580–596.
  32. Park, J.; Kahng, B.; Kamm, R. D.; Hwang, W. Atomistic Simulation Approach to a Continuum Description of Self-Assembled Beta-Sheet Filaments. *Biophys. J.* **2006**, *90*, 2510–2524.
  33. Christenson, H. K. Adhesion and Surface-Energy of Mica in Air and Water. *J. Phys. Chem.* **1993**, *97*, 12034–12041.
  34. de Gennes, P. G.; Brochard-Wyart, F.; Quéré, D. *Capillarity and Wetting Phenomena: Drops, Bubbles, Pearls, Waves*; Springer-Verlag: New York, 2003; p 291.
  35. Lamour, G.; Souès, S.; Hamraoui, A. Interplay between Long- and Short-Range Interactions Drives Neuritogenesis on Stiff Surfaces. *J. Biomed. Mater. Res., Part A* **2011**, *99A*, 598–606.
  36. Rivetti, C.; Guthold, M.; Bustamante, C. Scanning Force Microscopy of DNA Deposited onto Mica: Equilibration versus Kinetic Trapping Studied by Statistical Polymer Chain Analysis. *J. Mol. Biol.* **1996**, *264*, 919–932.
  37. Lara, C.; Usov, I.; Adamcik, J.; Mezzenga, R. Sub-Persistence-Length Complex Scaling Behavior in Lysozyme Amyloid Fibrils. *Phys. Rev. Lett.* **2011**, *107*, 238101.
  38. Sweers, K. K. M.; Bennink, M. L.; Subramaniam, V. Nanomechanical Properties of Single Amyloid Fibrils. *J. Phys.: Condens. Matter* **2012**, *24*, 243101.
  39. Zhou, X. F.; Cui, C. Y.; Zhang, J. H.; Liu, J. H.; Liu, J. S. Nanomechanics of Individual Amyloid Fibrils Using Atomic Force Microscopy. *Chin. Sci. Bull.* **2010**, *55*, 1608–1612.
  40. Guo, S. L.; Akhremitchev, B. B. Packing Density and Structural Heterogeneity of Insulin Amyloid Fibrils Measured by AFM Nanoindentation. *Biomacromolecules* **2006**, *7*, 1630–1636.
  41. Sweers, K.; van der Werf, K.; Bennink, M.; Subramaniam, V. Nanomechanical Properties of Alpha-Synuclein Amyloid Fibrils: A Comparative Study by Nanoindentation, Harmonic Force Microscopy, and Peakforce QNM. *Nanoscale Res. Lett.* **2011**, *6*, 270.
  42. Adamcik, J.; Lara, C.; Usov, I.; Jeong, J. S.; Ruggeri, F. S.; Dietler, G.; Lashuel, H. A.; Hamley, I. W.; Mezzenga, R. Measurement of Intrinsic Properties of Amyloid Fibrils by the Peak Force QNM Method. *Nanoscale* **2012**, *4*, 4426–4429.
  43. Castro, C. E.; Dong, J. J.; Boyce, M. C.; Lindquist, S.; Lang, M. J. Physical Properties of Polymorphic Yeast Prion Amyloid Fibers. *Biophys. J.* **2011**, *101*, 439–448.
  44. Kol, N.; Adler-Abramovich, L.; Barlam, D.; Shneck, R. Z.; Gazit, E.; Rousso, I. Self-Assembled Peptide Nanotubes Are Uniquely Rigid Bioinspired Supramolecular Structures. *Nano Lett.* **2005**, *5*, 1343–1346.
  45. Paparccone, R.; Ketten, S.; Buehler, M. J. Atomistic Simulation of Nanomechanical Properties of Alzheimer's A $\beta$ (1–40) Amyloid Fibrils under Compressive and Tensile Loading. *J. Biomech.* **2010**, *43*, 1196–1201.
  46. Xu, Z. P.; Buehler, M. J. Mechanical Energy Transfer and Dissipation in Fibrous Beta-Sheet-Rich Proteins. *Phys. Rev. E* **2010**, *81*, 061910.
  47. Sawaya, M. R.; Sambashivan, S.; Nelson, R.; Ivanova, M. I.; Sievers, S. A.; Apostol, M. I.; Thompson, M. J.; Balbirnie, M.; Wiltzius, J. J. W.; McFarlane, H. T.; *et al.* Atomic Structures of Amyloid Cross-Beta Spines Reveal Varied Steric Zippers. *Nature* **2007**, *447*, 453–457.
  48. Toyama, B. H.; Kelly, M. J. S.; Gross, J. D.; Weissman, J. S. The Structural Basis of Yeast Prion Strain Variants. *Nature* **2007**, *449*, 233–237.
  49. Wiltzius, J. J. W.; Landau, M.; Nelson, R.; Sawaya, M. R.; Apostol, M. I.; Goldschmidt, L.; Soriaga, A. B.; Cascio, D.; Rajashankar, K.; Eisenberg, D. Molecular Mechanisms for Protein-Encoded Inheritance. *Nat. Struct. Mol. Biol.* **2009**, *16*, 973–978.
  50. Relini, A.; Torrassa, S.; Ferrando, R.; Rolandi, R.; Campioni, S.; Chiti, F.; Gliozzi, A. Detection of Populations of Amyloid-Like Protofibrils with Different Physical Properties. *Biophys. J.* **2010**, *98*, 1277–1284.
  51. Solar, M.; Buehler, M. J. Comparative Analysis of Nanomechanics of Protein Filaments under Lateral Loading. *Nanoscale* **2012**, *4*, 1177–1183.
  52. vandenAkker, C. C.; Engel, M. F. M.; Velikov, K. P.; Bonn, M.; Koenderink, G. H. Morphology and Persistence Length of Amyloid Fibrils Are Correlated to Peptide Molecular Structure. *J. Am. Chem. Soc.* **2011**, *133*, 18030–18033.
  53. Petkova, A. T.; Leapman, R. D.; Guo, Z. H.; Yau, W. M.; Mattson, M. P.; Tycko, R. Self-Propagating, Molecular-Level Polymorphism in Alzheimer's Beta-Amyloid Fibrils. *Science* **2005**, *307*, 262–265.
  54. Smirnovas, V.; Baron, G. S.; Offerdahl, D. K.; Raymond, G. J.; Caughey, B.; Surewicz, W. K. Structural Organization of Brain-Derived Mammalian Prions Examined by Hydrogen-Deuterium Exchange. *Nat. Struct. Mol. Biol.* **2011**, *18*, 504–506.
  55. Cobb, N. J.; Apostol, M. I.; Chen, S.; Smirnovas, V.; Surewicz, W. K. Conformational Stability of Mammalian Prion Protein Amyloid Fibrils Is Dictated by a Packing Polymorphism within the Core Region. *J. Biol. Chem.* **2014**, *289*, 2643–2650.
  56. Singh, J.; Sabareesan, A. T.; Mathew, M. K.; Udgaonkar, J. B. Development of the Structural Core and of Conformational Heterogeneity during the Conversion of Oligomers of the Mouse Prion Protein to Worm-like Amyloid Fibrils. *J. Mol. Biol.* **2012**, *423*, 217–231.
  57. Kojima, H.; Ishijima, A.; Yanagida, T. Direct Measurement of Stiffness of Single Actin-Filaments with and without Tropomyosin by *in Vitro* Nanomanipulation. *Proc. Natl. Acad. Sci. U. S. A.* **1994**, *91*, 12962–12966.
  58. Gittes, F.; Mickey, B.; Nettleton, J.; Howard, J. Flexural Rigidity of Microtubules and Actin-Filaments Measured from Thermal Fluctuations in Shape. *J. Cell Biol.* **1993**, *120*, 923–934.
  59. Shen, Z. L.; Dodge, M. R.; Kahn, H.; Ballarini, R.; Eppell, S. J. Stress-Strain Experiments on Individual Collagen Fibrils. *Biophys. J.* **2008**, *95*, 3956–3963.
  60. Knowles, T. P. J.; Waudby, C. A.; Devlin, G. L.; Cohen, S. I. A.; Aguzzi, A.; Vendruscolo, M.; Terentjev, E. M.; Welland, M. E.; Dobson, C. M. An Analytical Solution to the Kinetics of Breakable Filament Assembly. *Science* **2009**, *326*, 1533–1537.
  61. Prusiner, S. B. A Unifying Role for Prions in Neurodegenerative Diseases. *Science* **2012**, *336*, 1511–1513.
  62. Sweers, K. K. M.; van der Werf, K. O.; Bennink, M. L.; Subramaniam, V. Spatially Resolved Frequency-Dependent Elasticity Measured with Pulsed Force Microscopy and Nanoindentation. *Nanoscale* **2012**, *4*, 2072–2077.

63. Guo, S. L.; Solares, S. D.; Mochalin, V.; Neitzel, I.; Gogotsi, Y.; Kalinin, S. V.; Jesse, S. Multifrequency Imaging in the Intermittent Contact Mode of Atomic Force Microscopy: Beyond Phase Imaging. *Small* **2012**, *8*, 1264–1269.
64. Proksch, R.; Yablon, D. G. Loss Tangent Imaging: Theory and Simulations of Repulsive-Mode Tapping Atomic Force Microscopy. *Appl. Phys. Lett.* **2012**, *100*, 073106.
65. Solares, S. D.; Chawla, G. Triple-Frequency Intermittent Contact Atomic Force Microscopy Characterization: Simultaneous Topographical, Phase, and Frequency Shift Contrast in Ambient Air. *J. Appl. Phys.* **2010**, *108*, 054901.
66. Ohi, M.; Li, Y.; Cheng, Y.; Walz, T. Negative Staining and Image Classification - Powerful Tools in Modern Electron Microscopy. *Biol. Proced. Online* **2004**, *6*, 23–34.